1.4 Methodology

Since the interferometric phase over coherent areas is mainly influenced by topography, deformation between the SAR acquisitions, and atmospheric delay, it is important to use SAR images over an area where either an accurate digital elevation model is available, or where there simply is minimal topography. The selected test sites in the Netherlands fulfill both requirements. Furthermore, a dense network of meteorological observation stations is available, providing a vast amount of significant meteorological data.

A set of *26 ERS SAR tandem pairs*, covering relatively flat areas centered around the Dutch provinces Groningen and Flevoland, is processed to phase unwrapped and geocoded interferograms.[2] *Meteorological data*, consisting of surface (synoptic) measurements, weather radar, radiosondes, and satellite imagery are used for the analysis of these interferograms. For each interferogram the type, extent and magnitude of local phase biases are evaluated. The hypothesis that this bias is of atmospheric origin is tested using meteorological data.

The project can be separated into two parts. The first part consists of the interferometric processing. The set of SLC (Single Look Complex) SAR data is processed to form geocoded, phase-unwrapped interferograms. The second part comprises the meteorological evaluation. Based on the acquisition dates and times, a set of meteorological data is composed, which enables the comparison and analysis with the observed phase artifacts in the interferograms. Finally, conclusions on the driving atmospheric mechanisms are presented.

1.5 Outline of this report

The report can be separated in a review part (chapter 2), a descriptive part (chapter 3 and 4), and a data analysis part (chapter 5). Based on existing literature, a brief résumé of the current status of the theoretical understanding of phase artifacts induced by the atmosphere is given in chapter 2. It describes the basic principles of SAR interferometry and radio wave propagation, and discusses some relevant atmospheric parameters.

Chapter 3 covers the interferometric database used in this specific study. It is described which interferometric processing steps are applied, and the necessary post-processing to obtain interpretable phase information. For this interpretation, a number of meteorological data sources are used. A description of these data, the instrumentation, and the obtained atmospheric parameters is the main topic in chapter 4.

The main analysis of the set of interferograms is performed in chapter 5. For every interferogram, the observed effects are discussed in both a descriptive and a quantitative way. Following this description, key points of the interpretation are described. It is tried to explain all observed effects from a meteorological point of view, and to define the driving mechanisms for the phase observations. Finally, some short conclusions on the discussed interferogram are drawn. The chapter concludes with a discussion, in which the results of the analyses are merged and evaluated statistically.

Finally, in chapter 6 the main conclusions and recommendations of the study are given on the type and magnitude of the phase anomalies and the feasibility of using meteorological

[2]Since one specific tandem acquisition was made during an extensive meteorological experiment (CLARA–Clouds and Radiation) in the western part of the Netherlands, which acquired a wealth of meteorological data, these data have also been evaluated.

data for estimating atmospheric disturbance.

1.5.1 How to read this report

While preparing this report, I found out that this work is perhaps not only interesting for scientists in the field of SAR interferometry. Apart from being a mere nuisance for applications of SAR interferometry in the generation of digital elevation models or differential deformation maps, the atmospheric signal observed in the SAR interferograms provides insights in the spatial distribution of water vapor, with an unsurpassed resolution level starting from 20×20 meters and a relative accuracy level of 1.8 mm signal delay. Therefore, this work might be of interest to meteorologists or, e.g., scientists working in the field of tropospheric modelling for high accuracy GPS applications.

The main purpose of this work is, however, the assessment of the atmospheric influence for ERS tandem SAR interferometry. Therefore, the used unit in the quantitative analyses is mostly radian or phase cycle. This can be easily transformed to millimeters water vapor delay in slant range using

$$1 \text{ rad} \approx 4.6 \text{ mm}, \quad \text{and} \quad 1 \text{ cycle} \approx 28 \text{ mm},$$

in which an accuracy level of 0.4 rad, or 1.8 mm, can be easily obtained. Mapping the slant range delay to the zenith direction, the values are 4.8 mm and 30 mm for radian and phase cycle respectively.

In the discussion of the interferograms, it was necessary to refer to a number of cities, regions, and meteorological stations in the Netherlands. To guide the reader unfamiliar with Dutch topography, schematic maps and short descriptions of the different regions are included at the beginning of the sections in chapter 5. Although the use of site specific names is avoided as much as possible, the reader is referred to those maps for assistance.

Chapter 2

Theoretical review

This chapter gives an introduction to some relevant topics considering SAR interferometry and the way it may be influenced by the atmosphere. The chapter starts with a brief review of the important equations governing the SAR interferometric configuration, and the way a localized atmospheric anomaly will affect it. The second section covers some aspects of radio wave propagation. It describes the importance of the refractive index and how a radio range error originates in the neutral atmosphere and in the ionosphere. Section 2.3 discusses some relevant physical characteristics of the troposphere and ionosphere, and lists some often used humidity measures. Finally, section 2.4 focuses on the specific consequences of atmospheric signal propagation for SAR interferometry. In this context, some important atmospheric phenomena are discussed in some more detail.
key words: SAR interferometry, atmosphere, radio range error, refractive index

2.1 SAR interferometry and atmospheric phase delay

Repeat pass SAR interferometry has been demonstrated by Li and Goldstein (1990) using Seasat SAR images. First applications for the generation of elevation models using ERS were performed by Zebker et al. (1994), whereas first accurate surface deformation maps were shown by Massonnet et al. (1993). Speculations on phase variations from atmospheric origin were published by Massonnet and Feigl (1995) and Massonnet et al. (1995).

The following paragraphs review the basic equations of repeat pass SAR interferometry, and describe how an atmospheric inhomogeneity will influence the observed interferometric phase.

2.1.1 Repeat pass SAR interferometry

The standard interferometric repeat pass configuration is shown in figure 2.1. At the positions 1 and 2 a phase measurement is made for a specific resolution cell. If the baseline B between the two antennas is divided into a perpendicular component $B^{\perp}$ and a parallel component $B^{||}$, these phase measurements can be written as

$$\psi_1 = \frac{4\pi}{\lambda} R_1, \quad \text{and} \tag{2.1}$$

$$\psi_2 = \frac{4\pi}{\lambda} (R_1 + B^{||}), \tag{2.2}$$

where R_1 is the slant range, measured by the time delay of that resolution cell, and λ is the wavelength of the signal. The far field approximation is used, implicating that the look angle θ is considered equal for sensor 1 and 2. No surface deformation terms are included in these equations.

The interferometric phase φ of the resolution cell is found by multiplying the complex value of image 1 with the conjugated complex value of image 2, which yields a phase difference

$$\varphi = \psi_1 - \psi_2 = -\frac{4\pi}{\lambda} B^{||}. \tag{2.3}$$

A value for $B^{||}$ can be found using the geometric relationship

$$B^{||} = B \sin(\theta - \alpha), \tag{2.4}$$

where α is the orientation of the baseline with length B.

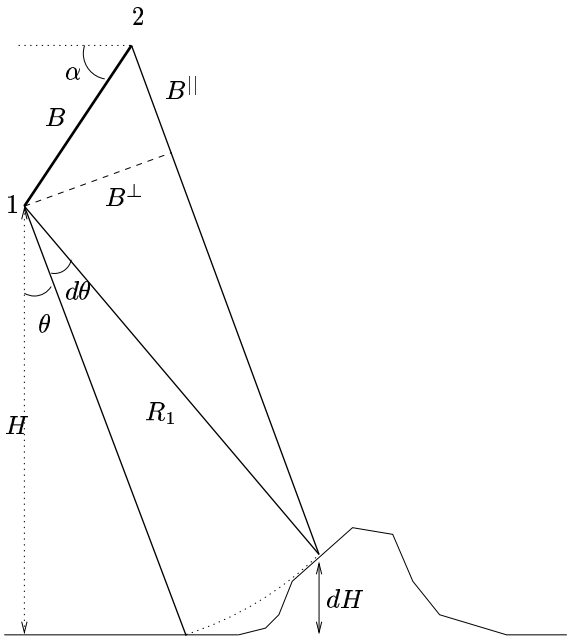

Figure 2.1 *Interferometric configuration*

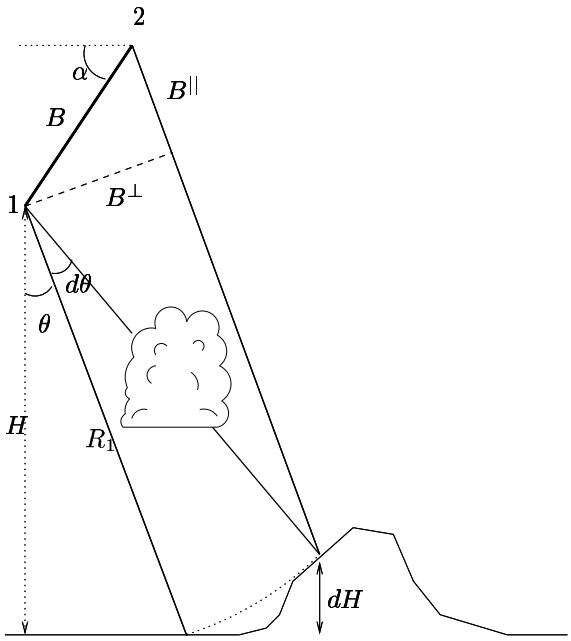

Figure 2.2 *A localized inhomogeneity*

The relationship with the topographic height is found using the height H of sensor 1 above a reference surface, i.e. the WGS84 ellipsoid. This sensor height is given by $H = R_1 \cos\theta$. The slant range R_1, however, cannot be used to uniquely determine the position of the resolution cell on Earth, see figure 2.1. Therefore, the change in look angle $d\theta$ connected with the topographic height dH needs to be determined from the interferometric measurement, using $dH = -R_1 \sin\theta d\theta$.

A change in look angle $d\theta$ yields a slight difference in the parallel baseline $dB^{||}$,

$$dB^{||} = B \cos(\theta - \alpha) d\theta, \tag{2.5}$$

which is consequently related to the observed change $d\varphi$ in the interferometric phase:

$$d\varphi = -\frac{4\pi}{\lambda} dB^{||}. \tag{2.6}$$

Using these equations, the relation between $d\varphi$, which is the measured phase difference between the reference phase and the observed phase of the resolution cell, and the topographic height dH, which is the height difference between a reference ellipsoidal height and the height of the resolution cell, can be written as

$$dH = \frac{\lambda}{4\pi} \frac{R_1 \sin\theta}{B\cos(\theta - \alpha)} d\varphi = \frac{\lambda}{4\pi} \frac{R_1 \sin\theta}{B^{\perp}} d\varphi. \tag{2.7}$$

The topographic height is therefore inversely proportional to the perpendicular baseline $B^{\perp}$. Note that when the parallel baseline is positive, as sketched in figure 2.1, a positive change in interferometric phase yields a positive topographic height (i.e. a hill instead of a valley). If the parallel baseline is negative, equation (2.7) will change in

$$dH = -\frac{\lambda}{4\pi} \frac{R_1 \sin\theta}{B^{\perp}} d\varphi, \tag{2.8}$$

and a positive phase results in a negative height.

2.1.2 The influence of an atmospheric inhomogeneity

The slant ranges in equation (2.1) and (2.2) are determined using the travel time τ of the signal and the velocity of light c, with

$$R = \tau c/2. \tag{2.9}$$

However, since the true velocity v of the radio waves in the atmosphere is slower than the velocity of light in vacuum c, an additional atmospheric delay term needs to be added, which can be translated to an (imaginary) excess distance ΔR_e:

$$\psi_1 = \frac{4\pi}{\lambda}(R_1 + \Delta R_{e,1}), \quad \text{and} \tag{2.10}$$

$$\psi_2 = \frac{4\pi}{\lambda}(R_1 + B^{||} + \Delta R_{e,2}). \tag{2.11}$$

Typical values for the excess distance are 2.5—3 meters. In the interferometric phase, cf. equation (2.3), this results in

$$\varphi = \frac{4\pi}{\lambda}(-B^{||} + \Delta R_{e,1} - \Delta R_{e,2}). \tag{2.12}$$

Assuming that the atmospheric delay is homogeneous for the whole SAR scene, the consequence of these excess distances is limited to a biased interferometric phase. As noted before, the main interferometric observable is a phase *change* ($d\varphi$), and therefore the atmospherically induced bias is eliminated.

However, the assumption of a homogeneous atmosphere is not valid for most of the areas in the world, were mixing processes cause localized temperature and humidity gradients, hereby inducing local differences in signal delay.

Figure 2.2 shows the same configuration as figure 2.1 with a localized atmospheric inhomogeneity at the time of the first SAR acquisition. It is assumed that the inhomogeneity is characterized by an increase in refractive index. This results in a slower propagation

velocity, or an increase in the excess distance $\Delta R_{e,1}$, with respect to the reference phase. Using equation (2.7) and (2.12), the interferometric phase can now be described by

$$d\varphi = \frac{4\pi}{\lambda}\left(\frac{B^{\perp}}{R_1 \sin\theta} dH + d\Delta R_{e,1} - d\Delta R_{e,2}\right). \tag{2.13}$$

In the example of figure 2.2, $d\Delta R_{e,2} = 0$, and therefore a localized signal delay at the first SAR acquisition will result in a positive phase change in the interferogram. A similar effect during the second SAR acquisition would cause a negative phase change. In contrary to the phase sign resulting from topographic height, atmospheric phase signs are *independent* of the parallel baseline[1].

Equation (2.13) clearly shows that the influence of localized signal delays on the interferometric phase is not related to the perpendicular baseline, in contrary to topographic height. Note that for a single-pass interferometer, the atmospherically induced delay (and the spatial delay variations) is equal for both receiving antennas, and is eliminated when differencing the two phase images.

In the approach used in this study, the value for dH in equation (2.13) is obtained from an a priori reference elevation model. Therefore, the first term in the brackets is known, and the topographic phase can be subtracted from the total phase, leaving

$$d\varphi = \frac{4\pi}{\lambda}\left(d\Delta R_{e,1} - d\Delta R_{e,2}\right), \tag{2.14}$$

which is referred to as the *differential interferogram* in the sequel. This simple equation describes the response of the interferometric phase φ on a signal delay $\Delta R_{e,i}$, for image i. It shows that, due to the relative character of the observations, it is only possible to measure spatial *variations* in signal delay. This is the reason why this study focuses on atmospheric *heterogeneities*, and not on the total atmospheric delay.[2]

From equation (2.13) it directly follows how atmospheric heterogeneities translate into DEM errors, if the two right terms of the equation would not be included in the model. An error in the DEM height ε_{dH} is related to a localized atmospheric delay $d\Delta R_e$ by

$$\varepsilon_{dH} = \pm\frac{R_1 \sin\theta}{B^{\perp}} d\Delta R_e \tag{2.15}$$

$$\approx \pm\frac{330000}{B^{\perp}} d\Delta R_e \tag{2.16}$$

where the sign is positive for a localized delay in the first acquisition, and negative for a localized delay during the second acquisition. Note that an increase in $B^{\perp}$ linearly suppresses the DEM errors caused by the atmospheric delays.

2.2 Radio wave propagation

The influence of the atmosphere on electromagnetic waves in the *microwave* band (1 GHz–30 GHz) can manifest itself in two forms (Hall et al., 1996), if we limit ourselves to Earth–

[1] Note that for negative parallel baselines, the absolute phase image might need to be reversed. This causes also the atmospheric signs to be reversed, which should be accounted for in the interpretation.

[2] It has to be noted that for areas with significant topography the vertical changes in atmospheric variability cannot be neglected anymore, as reported by, e.g., Delacourt et al. (1997), since changes in the vertical profile between the two acquisition dates result in a differential phase in the interferogram. These topographically induced atmospheric influences can, however, be neglected in the current study.

space configurations. First, there are the *clear air* effects of atmospheric gases and their associated refractive index changes, like signal delay, ray bending, absorption, reflection, and tropospheric scattering. Secondly, there are the effects of *liquid and solid particles* (clouds, precipitation, aerosols), like attenuation, cross polarization and scattering.

For the application of ERS tandem SAR interferometry, we will discuss signal delay in both forms: the clear air effects and the particle effects. In the following paragraphs, the clear air effects are considered. Particle effects are treated in the discussion on clouds and rain, later in this chapter.

2.2.1 The refractive index

For radio signals propagating through the atmosphere, the velocity and ray curvature is affected by variations in the refractive index n along the path. The refractive index is only slightly higher than the vacuum value ($n = 1$), and therefore often the scaled-up *refractivity*, N, is used, where $N = (n-1)10^6$. In the following paragraphs, the refractive index or the refractivity is expressed for the neutral atmosphere and the ionosphere. Since the neutral atmosphere cannot be modeled as a clear gas only for the purposes of this study, also the influence of clouds and precipitation is investigated

2.2.1.1 Neutral atmosphere

For radio frequencies up to 30 GHz in the troposphere, the refractivity N can be written as (Smith and Weintraub, 1953)

$$N = k_1 \frac{P_d}{T} + k_2 \frac{e}{T} + k_3 \frac{e}{T^2}, \tag{2.17}$$

where P_d is the partial pressure of dry air in mbar, e is the partial pressure of water vapor in mbar, and T is the absolute temperature in degrees Kelvin. The constants k_1, k_2, and k_3 have been first determined by Smith and Weintraub (1953). [$k_1 = 77.6$ K mb^{-1}, $k_2 = 71.6$ K mb^{-1}, and $k_3 = 3.75 \cdot 10^5$ K^2 mb^{-1}]. These constants are considered to be accurate to 0.5 % of N. The first term at the right hand side of equation (2.17) is often labeled as the "dry" delay, the two other terms as the "wet" delay. Assuming that the total atmospheric pressure $P = P_d + e$, and using the ideal gas law, an equivalent expression is obtained:

$$N = k_1 \frac{P}{T} + k_2' \frac{e}{T} + k_3 \frac{e}{T^2}. \tag{2.18}$$

In this expression, the first term at the right hand side is labeled the "hydrostatic" delay. The second term k_2' is defined as:

$$k_2' = k_2 - \frac{R_d}{R_v} k_1, \tag{2.19}$$

with $R_d = 287.053$ J K^{-1} kg^{-1}, and $R_v = 461$ J K^{-1} kg^{-1}. At saturation, the partial pressure of water vapor is typically less than 2.5% of the total atmospheric pressure, as given by the Clausius-Clapeyron equation, see section 2.3.3. For a temperature $T = 20$°C this equation yields the saturated partial water vapor pressure $e_s = 23.7$ mbar. A standard total atmospheric pressure $P = 1013$ mbar would now give the following components for equation (2.18): $N = 268.3 - 0.5 + 103.5 = 371$, or $(72\% - 0.1\% + 28\%)$. Using the total

atmospheric pressure in the first term at the right hand side we can estimate the one-way range delay in zenith direction using a simple barometric measurement, as described in section 2.2.2.

2.2.1.2 Ionosphere

The refractive index of the ionosphere can in first order be expressed by (Jakowski et al., 1992):

$$n = 1 - \frac{40.28}{f^2} \cdot EC, \tag{2.20}$$

where EC is the content of free electrons per cubic meter, and f is the frequency of the signal. Note the dispersive (frequency dependent) character of the ionospheric refractive index, as opposed to the non-dispersive neutral atmosphere.

2.2.2 The radio range error

The difference between the measured radio range R_e and the true slant range R_0 is called the radio range error ΔR_e, with

$$R_e = R_0 + \Delta R_e. \tag{2.21}$$

This error consists of a "bending" error and a propagation delay (Bean and Dutton, 1986). The *bending error* is the difference between the curved length of the ray path called the geometric range R_g and the true slant range R_0, denoted by ΔR_g. The *propagation delay* is the discrepancy between the velocity of propagation in vacuum and the lowered velocity of propagation in the refractive medium.

The geometric range R_g under a zenith angle θ, which is a function of height h, is given by:

$$R_g = \int_0^H \frac{1}{\cos\theta} dh, \tag{2.22}$$

and the measured radio range (including the delay *and* the bending effects) is given by

$$R_e = \int_0^H \frac{n}{\cos\theta} dh. \tag{2.23}$$

The total radio range error in (2.21) is therefore given by

$$\Delta R_e = \int_0^H \frac{n}{\cos\theta} dh - R_0, \tag{2.24}$$

or using the refractivity $N = (n-1) \times 10^6$

$$\begin{aligned} \Delta R_e &= 10^{-6} \int_0^H \frac{N}{\cos\theta} dh + (\int_0^H \frac{1}{\cos\theta} dh - R_0), \quad \text{or} \\ \Delta R_e &= \Delta R_N + \Delta R_g, \end{aligned} \tag{2.25}$$

where ΔR_N is the refractivity error (the propagation delay) and ΔR_g is the ray bending effect. Bean and Dutton (1986) have shown that even for extreme refractivities, the ratio

$\Delta R_g/\Delta R_e$ approaches zero for zenith angles less than 87°. Therefore, for the ERS look angle around 23°, the radio range error can be considered as a function of only the first integral in (2.25):

$$\Delta R_e = 10^{-6} \int_0^H \frac{N}{\cos\theta} dh. \tag{2.26}$$

The omission of factor 10^{-6} and the integral over dh gives

$$\Delta R_e \quad [\text{in mm}] = \frac{N}{\cos\theta} \quad [\text{per km}], \tag{2.27}$$

where the factor N can be used as an approximation for the one-way path delay in mm, per km of signal path.

2.2.2.1 Neutral atmosphere

Using equation (2.18) in (2.26), we find

$$\Delta R_e = \frac{10^{-6}}{\cos\theta} \left(k_1 R_d \int_0^H \rho dh + \int_0^H (k_2' \frac{e}{T} + k_3 \frac{e}{T^2}) dh \right). \tag{2.28}$$

The first term in the brackets is only dependent of the total density, and can be integrated assuming hydrostatic equilibrium. As the total surface pressure P_s can be written as

$$P_s = g_m \int_0^\infty \rho(z) dz, \tag{2.29}$$

where g_m is the approximate local gravity at the centroid of the atmospheric column (Saastamoinen, 1972), given by

$$g_m = 9.784 \cdot (1 - 0.0026 \cos 2\varphi - 0.00028 z_0) \quad [\text{m/s}^2], \tag{2.30}$$

dependent of surface height z_0 and latitude φ. Using this quantity, we can write the first term of (2.28) as the zenith ($\theta = 0$) hydrostatic delay (ZHD):

$$\Delta R_{e,\text{ZHD}} = k_1 \cdot 10^{-6} \cdot \frac{R_d}{g_m} P_s. \tag{2.31}$$

Using these parameters, and a surface pressure P_s measured with an accuracy of 0.4 mbar or better, this delay can be predicted with an accuracy of 1 mm or better (Bevis et al., 1996). For the test sites used in this study, $\Delta R_{e,\text{ZHD}} = 2.275 \cdot 10^{-3} P_s$.

The second term, the *wet path delay*, is dependent on the water vapor density and the temperature along the ray path. Without the term for the look angle, the *zenith wet delay* (ZWD) is

$$\Delta R_{e,\text{ZWD}} = 10^{-6} \int_0^H (k_2' \frac{e}{T} + k_3 \frac{e}{T^2}) dh. \tag{2.32}$$

This expression can directly be used for computing $\Delta R_{e,\text{ZWD}}$ from radiosonde observations (Bevis et al., 1996). Related useful parameters in this context are the vertically integrated water vapor and the precipitable water (PW), which is defined as the height of

an equivalent column of liquid water. Davis et al. (1985) introduced a *mean temperature*, defined as

$$\int_0^H \frac{e}{T} dh = T_m \int_0^H \frac{e}{T^2} dh, \tag{2.33}$$

which is approximated by Bevis et al. (1994) using the surface temperature T_s (Kelvin):

$$T_m = 0.72 T_s + 70.2. \tag{2.34}$$

Using the ideal gas law, the mean temperature T_m and equation (2.32), we find the zenith wet delay

$$\Delta R_{e,\mathrm{ZWD}} = 10^{-6} R_v (k_2' + k_3/T_m) \int_0^H \rho_v dh, \tag{2.35}$$

where R_v is the specific gas constant for water vapor (461 J K^{-1} kg^{-1}) and ρ_v the density of water vapor. The integrated water vapor is the integral at the right term of this equation. The precipitable water can be found by dividing the integrated water vapor by the density of (liquid) water ρ_w. This establishes the relation between the zenith wet delay and the precipitable water:

$$\Delta R_{e,\mathrm{ZWD}} = 10^{-6} \rho_w R_v (k_2' + k_3/T_m) \cdot \frac{1}{\rho_w} \int_0^H \rho_v dh \tag{2.36}$$

$$= \Pi^{-1} \mathrm{PW}, \tag{2.37}$$

where Π is a dimensionless quantity (Askne and Nordius, 1987). Following Bevis et al. (1992), $\Pi \approx 0.15$, but varies up to 10% due to changes in T_m, dependent on the location and the weather.[3] Using equation (2.36), either estimates of PW from numerical weather models, or measurements from water vapor radiometers can be used to determine the zenith wet delay.

Note that the water vapor density along the ray path is difficult to measure by traditional meteorological surface measurements, since there is little correlation between the water vapor density at the ground with that at higher altitudes, or at other positions horizontally (Reber and Swope, 1972).

2.2.2.2 Ionosphere

Inserting (2.20) in (2.26), and assuming no ray bending effects we find

$$\Delta R_e = \int_0^H \frac{(n-1)}{\cos\theta} dh = -40.28 \int_0^H \frac{EC}{f^2 \cos\theta} dh. \tag{2.38}$$

Note that an increase in the number of free electrons per m^2 causes an advance of the signal: the signal travels faster than c. The integration of the *free electron density* EC along the ray path represents the *total electron content* TEC, per m^2. Therefore we can express (2.38) as

$$\Delta R_e = \frac{-40.28}{f^2 \cos\theta} TEC. \tag{2.39}$$

[3] Use the k_1, k_2, and k_3 coefficients in Pa

The range error for the ERS SAR frequency can now be approximated by

$$\Delta R_e = -0.015 \cdot 10^{-16} \cdot TEC, \tag{2.40}$$

with TEC values vary between 0 at night to $20 \cdot 10^{16}$ m^{-2} at the minimum of the solar cycle to $100 \cdot 10^{16}$ m^{-2} at the maximum of the solar cycle, which corresponds to maximum delays of -30 cm and -1.5 m respectively.

2.3 Atmospheric structure

The main characteristics of the neutral atmosphere and the ionosphere are described in paragraphs 2.3.1 and 2.3.4 respectively. For the neutral atmosphere, a *standard atmosphere* describes the function of temperature and pressure with height. This model can be used to estimate the total radio range delay, and is described in paragraph 2.3.2. Since the main source of spatial variability of the refractive index is formed by heterogeneities in the moisture content, standard humidity measures need to be interpreted and converted to the partial water vapor pressure to solve equation 2.32 in section 2.2.2. An overview of different humidity measures and their conversions is given in paragraph 2.3.3.

2.3.1 The neutral atmosphere

The troposphere is the main region of the atmosphere, were masses of different kinds of air are very well mixed together, while the temperature decreases with altitude. Air is heated from the Earth surface, and the motions of the troposphere mix the heat energy. When parcels of air that are saturated with water vapor are moved into colder regions by the mixing, clouds are formed.

In the stratosphere, masses of air are still relatively well mixed, but the temperature increases with altitude. The gases are heated from below as well as from above. An ozone layer at approximately 50 km height causes the warming of the stratosphere with increasing height.

2.3.2 Standard atmosphere

The "1976 U.S. Standard Atmosphere" was developed as an engineering reference for the atmospheric state as a function of height (Stull, 1995). It describes the behavior of temperature and pressure in an idealized, dry, steady state atmosphere. The temperature equations are

$$\begin{array}{lcll} T & = & 288 + \alpha H & \text{for} \quad H < 11 \text{ km} \\ T & = & 216.5 & \text{for} \quad 11 \leq H \leq 20 \text{ km} \\ T & = & 216.5 + \beta(H - 20) & \text{for} \quad 20 < H < 32 \text{ km} \end{array} \tag{2.41}$$

with $\alpha = -6.5$ (K/km), $\beta = 1$ (K/km), and H the geopotential height. The geopotential height is defined to compensate for the decrease in gravitational attraction with the geometric height z, as

$$H = R_e z / (R_e + z) \tag{2.42}$$

where $R_e = 6356.766$ km is the mean Earth radius. Note that (2.41) uses the geopotential height in km.

Similar equations can be given for the standard atmosphere pressure P (in mbar):

$$\begin{array}{rcll} P & = & 1013.25(288.15/T)^{-5.255877} & \text{for} \quad H < 11 \text{ km} \\ P & = & 226.32\exp(-0.1568(H-11)) & \text{for} \quad 11 \leq H \leq 20 \text{ km} \\ P & = & 54.749(216.65/T)^{-4.16319} & \text{for} \quad 20 < H < 32 \text{ km} \end{array} \tag{2.43}$$

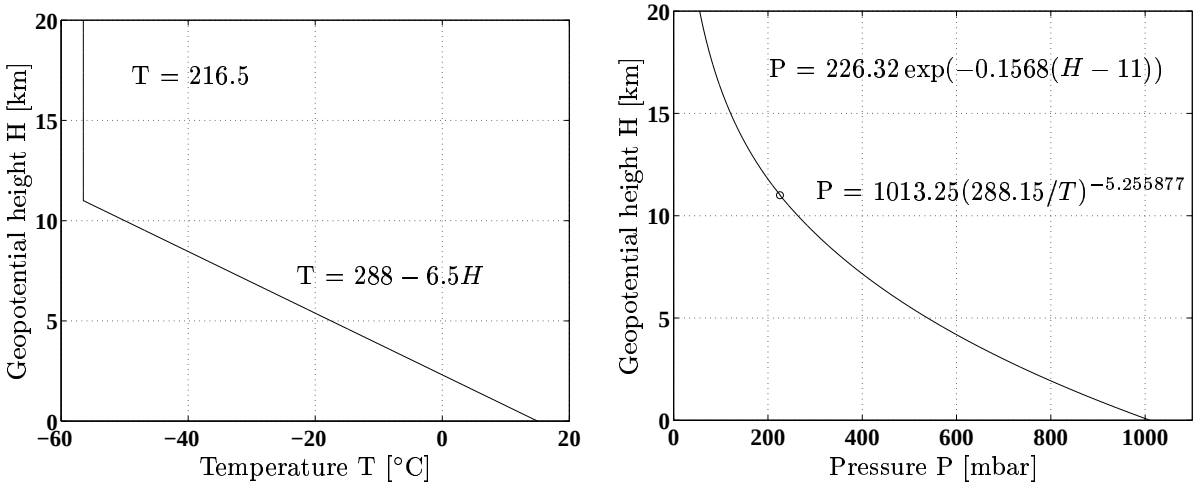

Figure 2.3 *The profiles of temperature and pressure in the 1976 U.S. Standard Atmosphere*

2.3.3 Humidity measures

A relationship which plays an important role in the definition of humidity is the *equation of state* for an ideal gas which has a meteorological form:

$$P_d = \rho_d R_d T, \tag{2.44}$$

where R_d is the *specific gas constant*, which is 287.053 J K^{-1} kg^{-1} for dry air, P_d is the pressure of the dry gas, ρ_d its density, and T the temperature in °K. Equation (2.44) is also known as the ideal gas law.

This equation of state can be used to calculate the *partial water vapor pressure* e as a function of the *absolute humidity* or vapor density ρ_v and the absolute temperature T, since vapor behaves as an ideal gas in terrestrial conditions:

$$e = \rho_v R_v T, \tag{2.45}$$

where R_v is the specific gas constant for water vapor, which is 461 J K^{-1} kg^{-1}. The ratio of the gas constants R_d/R_v is therefore 0.622, often represented by ϵ.

The absolute humidity ρ_v is an objective measure for the amount of water vapor (in grams of equivalent liquid water) per cubic meter air. There is an upper limit for the amount of water vapor that a parcel of air can absorb. An additional input of water vapor would lead to condensation into clouds (ice crystals or water droplets), fog, dew, etc. This maximal value, the saturation point or dew point, is dependent of the temperature. Warm air can absorb more water vapor than cold air: it has a higher saturation point, cf. table 2.1. The saturation partial water vapor pressure e_s at temperature T is described by the

Air temp [°C]	Absolute humidity [grams/m^3]
0	4.8
10	9.4
20	17.3
30	30.4

Table 2.1 *The relation between the air temperature and amount of liquid water a cubic meter air can absorb.*

Clausius-Clapeyron equation (Stull, 1995):

$$e_s = e_0 \exp\left(\frac{L}{R_v}(\frac{1}{T_o} - \frac{1}{T})\right), \tag{2.46}$$

where $e_0 = 6.11$ mbar, $T_0 = 273$ °K, and L is the latent heat. Over a flat water surface, $L = 2.5 \cdot 10^6$ J kg^{-1}, which is the latent heat of vaporization. In this case, cloud droplets are being formed. Over a flat ice surface, $L = 2.83 \cdot 10^6$ J kg^{-1}, which is the latent heat of deposition, when ice crystals are being formed. For a temperature of 20 °C, $e_s = 23.7$ mbar, roughly 2.3 percent of the average total atmospheric pressure of 1013 mbar. Note that e_s does not depend on the pressure.

The *relative humidity* RH is the ratio of the amount of water vapor in the air compared to the saturation amount of water vapor at that temperature: $RH = (e/e_s) \cdot 100\%$ For all practical purposes the relative humidity in water clouds is 100 percent. The partial pressure of water vapor e can be computed from the relative humidity RH and the temperature T, using equation (2.46):

$$e = \frac{RH}{100} e_s(T). \tag{2.47}$$

The humidity *mixing ratio* r is the ratio between the mass of water vapor and the mass of dry air:

$$r = \frac{m_v}{m_d} = \frac{\epsilon \cdot e}{P_d} \tag{2.48}$$

The ratio between the mass of water vapor and the *total* pressure is called the *specific humidity*:

$$q = \frac{m_v}{m_d + m_v} = \frac{\epsilon \cdot e}{P_d + e} \tag{2.49}$$

As an example, for typical low tropospheric conditions, $q = 10$ g kg^{-1}, and $P_d + e = 1000$ mbar, so the partial pressure of water vapor $e = 16$ mbar.

The *precipitable water content* is the total amount of water vapor in a vertical column of the atmosphere, if it would all condense, see also section 2.2.2.

2.3.4 The ionosphere

The ionosphere can be characterized by the ability of external sources to "knock-off" electrons from atoms, hereby creating *free* electrons which are not bound to their remaining

ions. These external sources are mainly the solar ultraviolet and Röntgen radiation and energetic electrons of solar and magnetospheric origin. The number of (free) electrons is represented by the *electron density*, in electrons per m^3.

Although the electron density is temporally and spatially variable, the ionosphere is often treated as a spherical shell between 60 and 600 km height with a *constant* electron density in height for a certain time t. Radio signals traversing through the ionosphere are dispersively delayed along their paths by interactions with the free electrons. A dispersive delay means that the signal delay is frequency dependent, which is the key for, e.g., GPS or radar altimetry (dual-frequency) to estimate the ionospheric (or plasma) delay.

Physically, the ionospheric delay is a path integral through the ionospheric electron density. This integral therefore has the dimension electrons per m^2, and is commonly known as the Total Electron Content or TEC. If the path integral is taken in the zenith direction it is also known as the Vertical TEC (VTEC). To achieve favorable quantities, one TEC unit (TECU) is defined as:

$$1\text{TECU} = 10^{16} \frac{\text{electrons}}{\text{m}^2} \tag{2.50}$$

The delay of a radio wave, propagating through the ionosphere, is different for the phase and the group velocity. Phase delay depends on electron content and affects carrier signals. Group delay depends on dispersion in the ionosphere as well, and affects signal modulation, i.e. the codes on GPS signals. The phase and group delays are of the same magnitude but opposite sign.

Two-hourly maps of the Vertical TEC for Europe are shown in figure 2.4, using dual frequency GPS observations collected by the IGS[4] network, provided by the DLR Remote Sensing Ground Station Neustrelitz. In this figure, apart from the normal diurnal variation, an ionospheric storm is visible as well (Ho et al., 1998).

Ionospheric gravity waves occur, e.g., when a sudden disturbance in ion density (e.g., a solar eclipse, waves over a mountain edge, heavy thunderstorms, earthquakes or rocket launches) triggers an expanding wave front. These wave normally have enormous wavelengths (hundreds of kilometers), and have gravity as restoring force. Cheng and Huang (1992) reported waves with a wavelength between 160 and 435 km after the eruption of Mount Pinatubo in 1991.

The ionosphere can be divided in a number of layers, which have different characteristics. The D-layer (80–100 km) receives only a minor part of the solar radiation, since most of the energy has been absorbed by higher ionospheric layers, and is therefore only weakly ionized. After sunset, this layer disappears completely. The E-layer (100–140 km) has little more ionization, but mostly fades into the F1-layer at night. The F1 and F2 layers, are located at 140–200, and 200–400 km respectively. Traveling Ionospheric Disturbances (TIDs) occur mainly in the F-layers. Large scale TIDs have wavelengths of 100–1000 km, and medium scale TIDs have wavelengths of approximately 100 km (Afraimovich et al., 1992).

[4]International GPS Service for Geodynamics

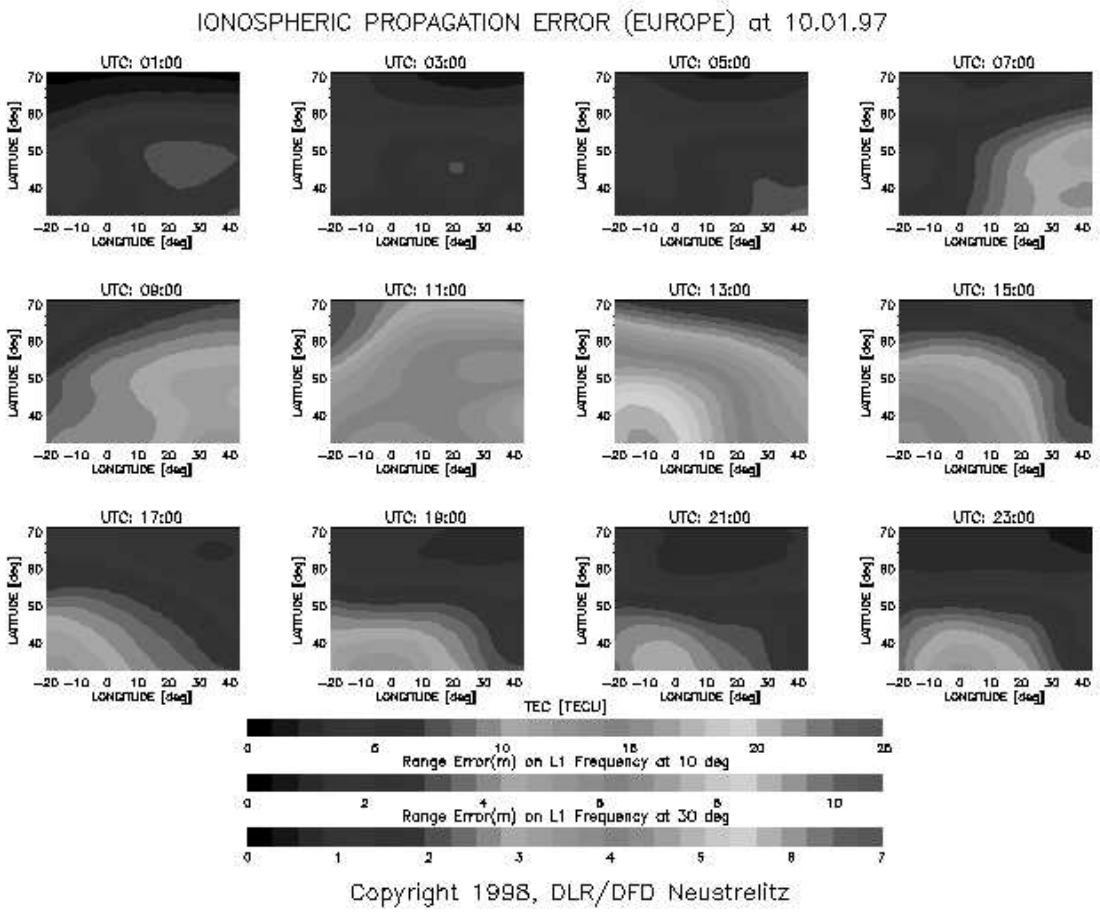

Figure 2.4 *Ionospheric map for 10 January 1997, (DLR Neustrelitz). The subimages show the two-hourly change in TEC from 1:00 UTC to 23:00 UTC. The daily variation can be observed as well as an ionospheric storm over south Spain and Morocco. The lower two colorbars give the range error for the two GPS frequencies, L_1 and L_2, showing the dispersive nature of the ionosphere.*

2.4 Signal propagation characteristics for SAR interferometry

Range errors described in literature are often described as a single ray, one way, zenith delay in meters. To assess their influence on SAR interferometry, some specific characteristics of the interferometric configuration need to be considered. A three step model is proposed to translate range errors to atmospheric errors in SAR interferograms:

Step 1 The zenith range error for a single ray, one way delay $\Delta R_e^z(x, y, t_1)$ at horizontal position (x, y) and time t_1, is mapped to an incidented, two way phase delay $\psi_1(x, y)$. A simple mapping function $1/\cos\theta$, where θ is the SAR look angle, and multiplication factor two yield[5]

$$\psi_1(x, y) = 2 \times \frac{1}{\cos\theta} \frac{2\pi}{\lambda} \Delta R_e^z(x, y, t_1). \tag{2.51}$$

[5]More sophisticated mapping functions such as described in (Niell, 1996) differ from $1/\cos\theta$ up to 1–1.5%.

Step 2 The two way single ray delay is extended to a multiple rays delay field, covering the full SAR scene. Due to the wrappedness of the phase, only the gradients $\partial/\partial x$ and $\partial/\partial y$ can be found. In x-direction this can be written as

$$\frac{\partial \psi_1(x,y)}{\partial x} = \frac{4\pi}{\lambda \cos\theta} \frac{\partial \Delta R_e^z(x,y,t_1)}{\partial x} \tag{2.52}$$

Step 3 The multiple ray, two way incidented delay of the first acquisition is differenced with that of the second acquisition. With $\varphi = \psi_1 - \psi_2$, this results in

$$\frac{\partial \varphi(x,y)}{\partial x} = \frac{4\pi}{\lambda \cos\theta} \left(\frac{\partial \Delta R_e^z(x,y,t_1)}{\partial x} - \frac{\partial \Delta R_e^z(x,y,t_2)}{\partial x} \right). \tag{2.53}$$

From equation (2.53) it follows that the total vertical delay $\Delta R_e^z(x,y,t)$ is eliminated, and a double-difference observable is obtained: the difference between two horizontal gradient fields.

Note that there is an inherent conflict in this representation. The mapping function assumes a horizontally layered isotropic atmosphere, whereas the main interferometric observable is in fact the horizontal variation! Unless a detailed 3D refractivity field is available at the SAR acquisitions, there is no solution for this problem. It will, therefore, cause a horizontal shift of the phase artifacts with respect to the location of the physical atmospheric anomalies. This shift Δx can be estimated using the average expected height H of the physical anomaly by:

$$\Delta x = H \tan\theta \approx 0.4 \cdot H. \tag{2.54}$$

In the following paragraphs some selected topics will be discussed, which can be of direct influence in SAR interferograms. Paragraph 2.4.1 reviews some results regarding horizontal gradients in tropospheric delay, and paragraphs 2.4.3 and 2.4.4 describes earlier findings on delay caused by rain and frontal zones respectively. Paragraph 2.4.5 describes some basic ideas of turbulence theory and how radially averaged spectra can be used to get an indication of the spectral characteristics of the observed differential interferograms. Finally, paragraph 2.4.6 and 2.4.7 address the ionospheric effects, first by giving a rule of thumb to assess the influence of the ionosphere, and second to distinguish between tropospheric and ionospheric effects.

2.4.1 Horizontal tropospheric delay gradients

Radiometer observations carried out by Alber et al. (1997) over a 43 km horizontal baseline give an indication of the horizontal gradient of the wet delay for a continental test site. A maximal wet zenith delay difference of 60 mm was observed. Davis et al. (1991) reported similar wet delay gradients for a coastal site: 0.1–1 N-units per km, cf. equation 2.27. Alber et al. (1997) observed pressure gradients of 1 mbar using plain barometric observations, which would correspond to a zenith dry delay gradient of approximately 3 mm. In their experiments, the maximum wet delay gradients were approximately 20 times larger than those from dry gradients.

2.4.2 The influence of clouds

Hall et al. (1996) have listed the liquid water content of clouds, see table 2.2. The maximum of the liquid water content is found at about 2 km above the cloud base. The liquid water content, W, can be related to the dielectric refractivity using the Clausius-Mossotti equation, (Solheim et al., 1997):

$$N_{\text{cloud}} = \frac{3}{2}\frac{W}{\rho_w}\frac{\varepsilon_0 - 1}{\varepsilon_0 + 2}, \tag{2.55}$$

where ε_0 is the permittivity of water and ρ_w is the density of liquid water. This relation is independent of the shape of the cloud droplet (Born and Wolf, 1980). Although the permittivity of water is a weak function of temperature, it is possible to approximate equation (2.55) to within 1% (Solheim et al., 1997) as:

$$N_{\text{cloud}} = 1.45W. \tag{2.56}$$

Since the value of N_{cloud} reflects the difference with the vacuum refractive index, equation (2.27) can be used to determine the additional delay $\Delta R_{e,\text{cloud}}$ caused by the liquid water in clouds:

$$\Delta R_{e,\text{cloud}} \quad [\text{in mm}] = \frac{1.45}{\cos\theta} W \quad [\text{per km}]. \tag{2.57}$$

Note that cloud droplet refractivity is in fact *dispersive*. However, since the dispersive part of the refractivity is much smaller than the non-dispersive part it can be ignored for C-band frequencies.

Type of cloud	Liquid water content [g/m^3]	Zenith delay [mm/km]
Stratiform clouds	0.05–0.25	0.1–0.4
Small cumulus clouds	0.5	0.7
Cumulus congestus and cumulonimbus	0.5–2.0	0.7–3
Ice clouds	< 0.1	< 0.1

Table 2.2 *Liquid water content in clouds, after Hall et al. (1996) and Bean and Dutton (1986)*

Table 2.2 shows the zenith delay for the four mentioned cloud groups. For repeat pass SAR interferometry, stratiform clouds and ice clouds do not cause large phase disturbances, due to their large horizontal extent and small additional delay. However, especially the cumulus type of clouds can result in significant additional phase delay, as they have a relatively limited horizontal size combined with a large vertical height and liquid water content.

2.4.3 The influence of rain

Rain characteristics can be divided into two types (Goldhirsch and Rowland, 1982): stratiform rain (non-convective), and thunderstorm (convective). Stratiform rains are generally widespread (hundreds of kilometers) and have rain rates of less then 20 mm/hr. This type of rain is assumed to fall from near the 0°C isotherm. This implies rain fall paths of 4–5 km in summertime (for latitudes of 15–45° north). Convective rain cells have a horizontal

extent in the order of kilometers and many of these cells can occur embedded in a thunderstorm. In this type of rain, drops are often carried in a supercooled state to several km above the 0° isotherm. The rain fall path can be up to 10 km.

Rogers and Olsen (1975) have published curves which express the relationship between the range error through rain as a function of the rain rate in mm/hr, see figure 2.5, based on experimental results. From these curves it follows that for a 5 km nadir rain path and a 100 mm/hr rain (thunderstorm), the range error for a two way path is 5 cm. For a stratiform type of rain with 10 mm/hr (moderate rain) over a 5 km path, the two-way range error is 1 cm (Goldhirsch and Rowland, 1982). Since the convective rains are much more localized, they will cause larger gradients and will be more prominently visible in the interferograms. The results from Rogers and Olsen (1975) were obtained at 6 GHz, but are expected to deviate little for the 5.3 GHz frequency of the ERS SAR.

The correspondence between the size (diameter) of the rain cells and the rain rate is studied by Edgar et al. (1973), and Nathanson (1969), and the results are shown in figure 2.6. It is found that rainfall diameters of 20 km and larger have rainfall rates of

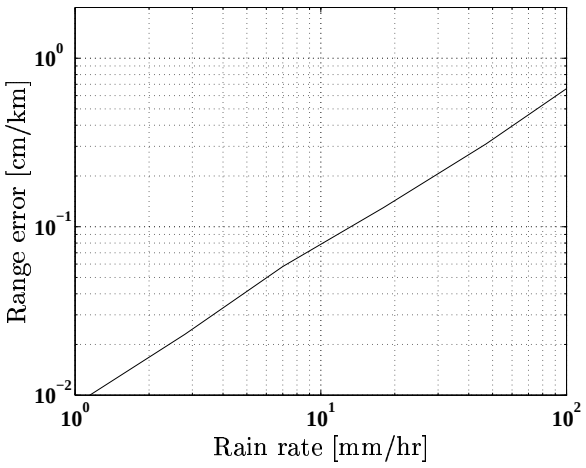

Figure 2.5 *One way range error per km through uniform rain. Curves are adapted from Rogers and Olsen (1975) (Goldhirsch and Rowland (1982))*

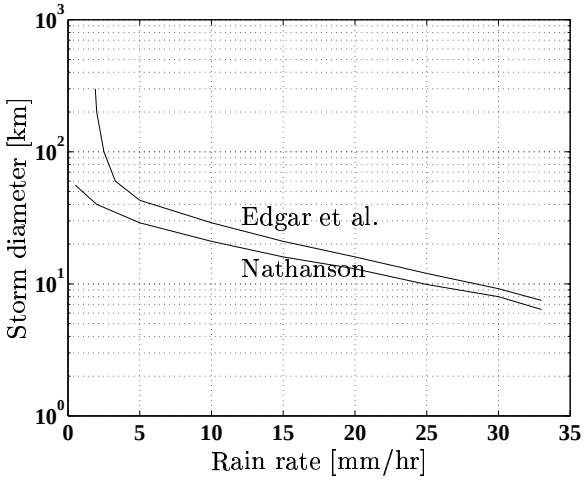

Figure 2.6 *Storm diameter versus rainfall rate, according to Edgar et al. (1973) (the upper profile), and Nathanson (1969) (the lower profile)*

10–15 mm/hr or less. Larger rain rates are confined within smaller diameters. Crane (1996) gives an extended overview of the statistics and structure of rain.

2.4.4 The influence of frontal zones

High and low pressure centers (highs and lows) cause circulation patterns of the surrounding air masses. Highs are characterized by downward motion (*subsidence*) aloft, and horizontal spreading air (*divergence*) near the surface. Winds are mostly light, and cloud development is impeded. Fronts are usually associated with lows, and two fronts per low are most common, a cold front and a warm front(Stull, 1995).

Fronts mark the boundaries between air masses. Important attributes are (Stull, 1995):

- strong horizontal temperature, moisture and wind gradients,

- strong vertical shear of the horizontal wind,
- relative minimum of pressure, and
- clouds and precipitation.

Along a cold front there are narrow bands of cumuliform clouds, with possible thunderstorms (Cb's) and scattered showers. The winds are stronger and gusty, and the pressure reaches a relative minimum. On the northern hemisphere, wind shifts and advects colder air from the north. As this cold air advects over the warmer ground, it becomes unstable, convective, and very turbulent. Warm fronts are more spatially extended. The leading edge of the front is formed by cirrostratus clouds, followed by altostratus, stratus, and possibly nimbostratus clouds which form a rain band.

A simulation of the effect of a cold front on the interferometric phase can be performed using the distribution of the refractivity around an idealized cold front, as described in Bean and Dutton (1986). The cold front is shown in figure 2.7, where the fat line indicates the cold front, and the isopleths are lines of equal refractivity N. The one-way zenith

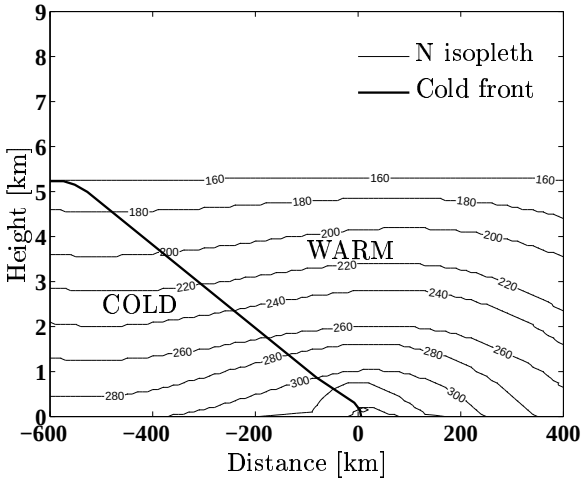

Figure 2.7 *Refractivity isopleths over an idealized cold front. The diagonal line indicates the position of the front.*

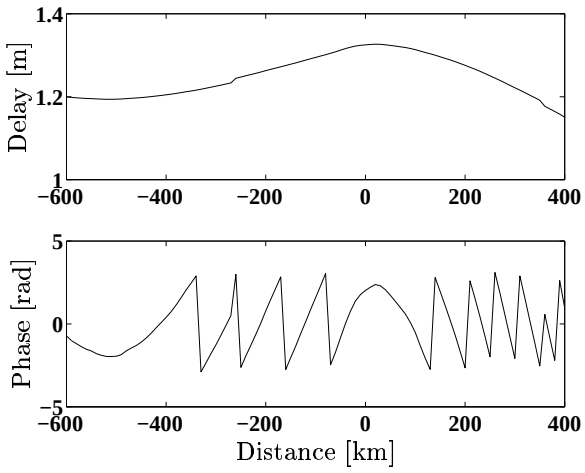

Figure 2.8 *One way zenith delay, and its result on the two-way incidented interferometric phase, caused by the cold front.*

delay caused by the lower half of the cross section is shown in figure 2.8, just over the simulated interferometric phase, assuming a second image with horizontal homogeneous layers, and a look angle of 23 degrees. For distances within 100 km, the front results in at most one cycle phase variation, with a phase "hump" just over the surface front.

2.4.5 Turbulence measures

Atmospheric turbulence causes refractive index fluctuations, causing phase fluctuations in SAR interferograms. The effects of turbulence can be modeled in terms of Kolmogorov theory.

In the Kolmogorov theory the dynamics of refractive index fluctuations are used to predict the properties of phase distortions introduced into a wave propagating through turbulence.

Kolmogorovs theory of turbulence predicts that refractive index fluctuations can only come about in a specific way - that is, they have well defined statistics which are weighted only by a single parameter - the strength of turbulence (C_N^2).

The *turbulence structure function* for a 3-D refractivity field, is defined as (Treuhaft and Lanyi, 1987)(Ruf and Beus, 1997):

$$D_N(s) = \mathrm{E}\{(N(\vec{x}) - N(\vec{x}+\vec{s}))^2\} \tag{2.58}$$

where $N(\vec{x})$ is the refractivity at $\vec{x}$, s is the magnitude of the separation between the points and E denotes the expectation over all realizations of the random function $N(\vec{x})$. While the separation s lies within the inner and outer limits of isotropic turbulence, Kolmogorov turbulence theory predicts (Tatarski, 1961);

$$D_N(s) = C_N^2 s^{2/3}, \tag{2.59}$$

where C_N^2 is the structure constant.

When measuring the integrated refractivity along a vertical path through the atmosphere, the separation s can only be determined in the horizontal plane. Using the range error $\Delta R_e = 10^{-6}\int_0^H N dh$ as main observable, a turbulence structure function can be defined for the (horizontal) range error field as for the 3-D refractivity field:

$$D_{\Delta R_e}(s) = \mathrm{E}\{(\Delta R_e(\vec{x}) - \Delta R_e(\vec{x}+\vec{s}))^2\} \tag{2.60}$$

For separations s within the inner and outer scales of isotropic turbulence, Kolmogorov theory predicts the relationship (Tatarski, 1961):

$$D_{\Delta R_e}(s) = C_{\Delta R_e} s^{5/3}. \tag{2.61}$$

According to Ruf and Beus (1997) the factor 5/3 decreases to 0 as s reaches the outer scale of turbulence. An estimate of the power law dependence can be found using a log/log linear regression of $D_{\Delta R_e}(s)$ versus s:

$$\log(D_{\Delta R_e}(s)) = \beta \log(s) + \log(C_{\Delta R_e}). \tag{2.62}$$

where β should approach 5/3 for regions of turbulence.

2.4.5.1 Relation between the structure function and the radial averaged spectrum

Following the derivation of Tatarski (1961), the spatial structure function can be defined as

$$\begin{aligned} D_f(r) &= \mathrm{E}\{(f(x+r) - f(x))^2\} && (2.63)\\ &= \mathrm{E}\{(f(x+r)^2\} + \mathrm{E}\{(f(x)^2\} - 2\mathrm{E}\{f(x+r)f(x)\} && (2.64)\end{aligned}$$

If $R_f(r)$ is the autocorrelation function, we can write 2.63 as

$$D_f(r) = 2(R_f(0) - R_f(r)). \tag{2.65}$$

As long as $R_f(\infty) = 0$, this means that $D_f(\infty) = 2R_f(0)$, and we can describe the autocorrelation function in terms of the structure function

$$R_f(r) = \frac{1}{2}D_f(\infty) - \frac{1}{2}D_f(r). \tag{2.66}$$